iScience

CellPress
OPEN ACCESS

Article

Co-utilization of wastewater sludge and heavy metals for single-atom electrocatalytic reduction of gaseous CO_2

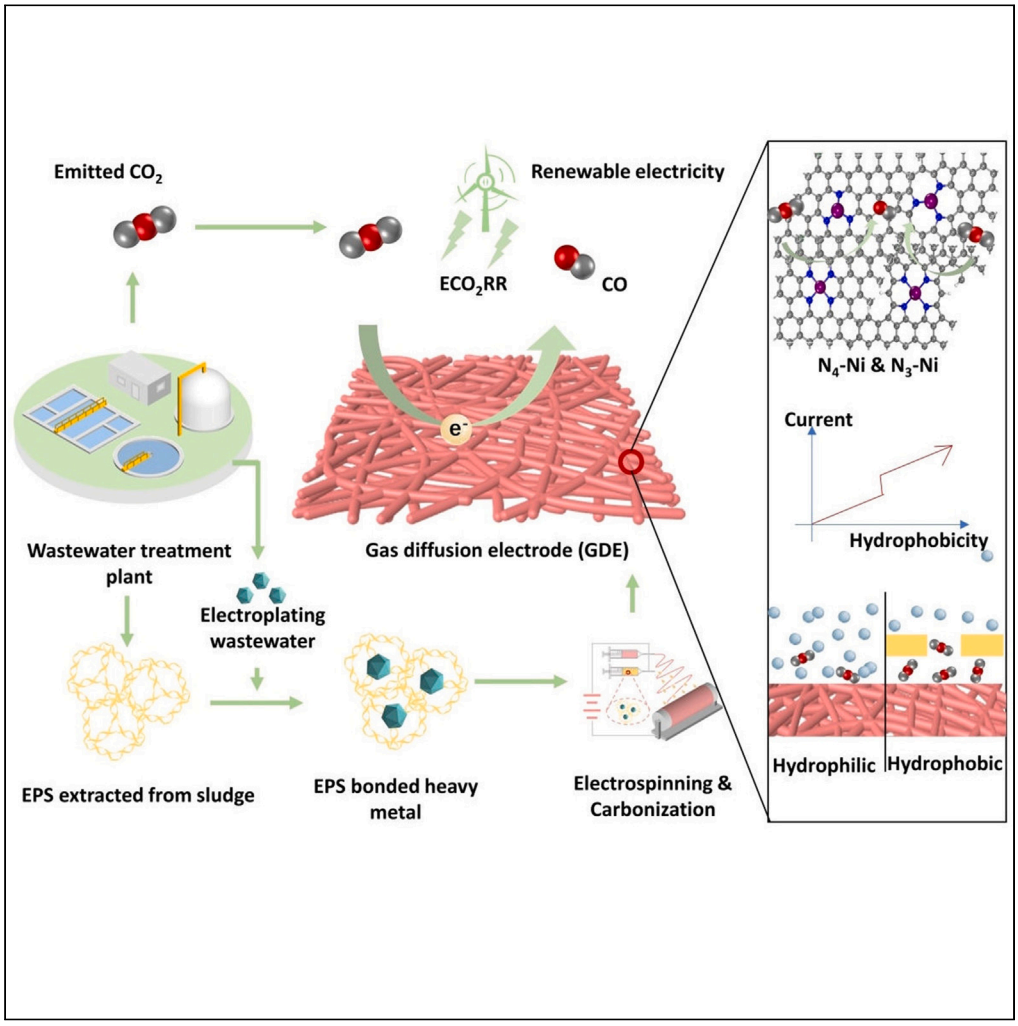

Baiqin Zhou, Zhida Li, Xinyue He, ..., Guifeng Li, Ziqi Zhang, Lu Lu

lulu@hit.edu.cn

Highlights

The utilization of sludge and heavy metal wastewater to convert CO_2

EPS atomically disperse Ni onto an integrated gas diffusion electrode

N-enriched wastes are competitive to synthesize efficient Ni single atom catalysts

Protein of EPS plays the biggest role in synthesizing N_x-Ni coordination

Zhou et al., iScience 27, 109956
June 21, 2024
https://doi.org/10.1016/j.isci.2024.109956

iScience

CellPress
OPEN ACCESS

Article

Co-utilization of wastewater sludge and heavy metals for single-atom electrocatalytic reduction of gaseous CO_2

Baiqin Zhou,[1] Zhida Li,[1] Xinyue He,[1] Chunyue Zhang,[1] Shanshan Pi,[1] Min Yang,[1] Wei Zhang,[1] Guifeng Li,[1] Ziqi Zhang,[1] and Lu Lu[1,2,*]

SUMMARY

Synergetic management of waste activated sludge, heavy metals (HMs) and CO_2 for their valorization and cyclic utilization is rarely reported. Herein, we employed sludge-derived extracellular polymeric substances (EPS) and HMs in wastewater to fabricate a gas diffusion electrode (GDE) for electrochemical CO_2 reduction. This approach atomically dispersed Ni at each nanofiber of the GDE. Abundant N element in the EPS proved to play a key role in the formation of N_x-Ni (mixture of N_3-Ni and N_4-Ni) sites for highly efficient CO_2 to CO conversion. The atomical Ni^{3+} shows high catalytic activity. Direct gaseous CO_2 reduction in a membrane electrode assembly generated a current density up to 50 $mA \cdot cm^{-2}$ with CO:H_2 ratio of ~100 and ~75% FE_{CO} under 2.69 cell voltage. This strategy takes advantage of all waste streams generated on site and consolidates traditionally separated treatment processes to save costs, produces value-added products and generates carbon benefits during wastewater treatment.

INTRODUCTION

Current wastewater treatment leads to intensive energy consumption (~3% global electricity),[1] huge waste activated sludge (WAS) production (global 136 million tons)[2] and considerable greenhouse gas (GHG) emission (~1.6% global GHG emission) annually.[1] For achievement of sustainable development and "carbon neutral" pledge, therefore, more efforts should be made to synergize mitigation of both wastes and carbon emission during wastewater treatment. Renewable grids driven electrochemical CO_2 reduction reaction (ECO_2RR) using single atoms catalysts (SACs), with the maximum catalytic sites and tunable electronic structures, holds a great potential for CO_2 mitigation and valorization (value-added chemicals production) in wastewater treatment industries,[3–5] such as converting abundant CO_2 (30–40% content) in biogas of WAS digestion to valuable products. Since the early reports on the introduction of SACs on ECO_2RR,[6–8] great efforts have been made to advance the CO_2 turnover efficiency and duration of SACs. Yang et al.[8] first demonstrated the improvement of CO_2 to CO conversion by Ni SACs due to their specific electronic structure. The smallest catalytic sites in atomic level delivered the optimal CO_2 conversion, and the current news even reported that ~100% CO_2-CO conversion at long-term operations.[3] However, large-scale application of SACs for ECO_2RR is still challenged due to complicated and high-cost synthesis of materials, despite it has been extensively studied in the lab.[9–11] Recently, low-cost carbon matrices and earth-abundant metals show great potential for fabricating SACs.[3,12,13] Given WAS has served as a good organic adsorbent/carbon matrix for binding various heavy metals (HMs) in wastewater,[14–16] we suppose whether it is feasible to employ it to manufacture SACs for *in situ* ECO_2RR and waste reclamation, achieving waste-to-wealth. So far, there have been few reports on this route.

Although SACs can be fabricated using low-cost carbon matrices, such as carbon black[3] and biochar[12,13] etc., the defined SACs need the coordination structure between HMs and the N-contained functional groups, which is crucial to the catalytic activity.[3–5] Thus, the SACs preparation by these low-cost materials requires introduction of quantitative N-contained chemicals, such as melamine[13] and urea.[3] As a natural polymer, extracellular polymeric substances (EPS) secreted by microorganisms is abundant in WAS[14–16] and has been shown to serve as an efficient bio-adsorbent for HMs adsorption with high adsorbing capacity.[17,18] The abundant C- and N-contained functional groups in EPS may serve as desirable sites for HMs anchoring inside the EPS cage, presenting a similar structure to the highly efficient SACs.[5,17–19] This may allow to center metals in the ligand with well-defined N coordination that will benefit adsorption or desorption of ECO_2RR intermediates, and thus lowering the energy barriers. Recent studies show that SACs based on earth-abundant metals also lead to highly efficient ECO_2RR.[4,19] For instance, Ni SACs with well-defined N coordination presents comparable selectivity (~95% Faradaic efficiency, FE) to the precious metals for CO_2 to CO conversion,[3,5,19,20] where N_x-Ni is the key site for CO_2 reduction and exhibits weak CO binding energy to facilitate the

[1]State Key Laboratory of Urban Water Resource and Environment, School of Civil and Environmental Engineering, Harbin Institute of Technology, Shenzhen, Shenzhen 518055, China
[2]Lead contact
*Correspondence: lulu@hit.edu.cn
https://doi.org/10.1016/j.isci.2024.109956

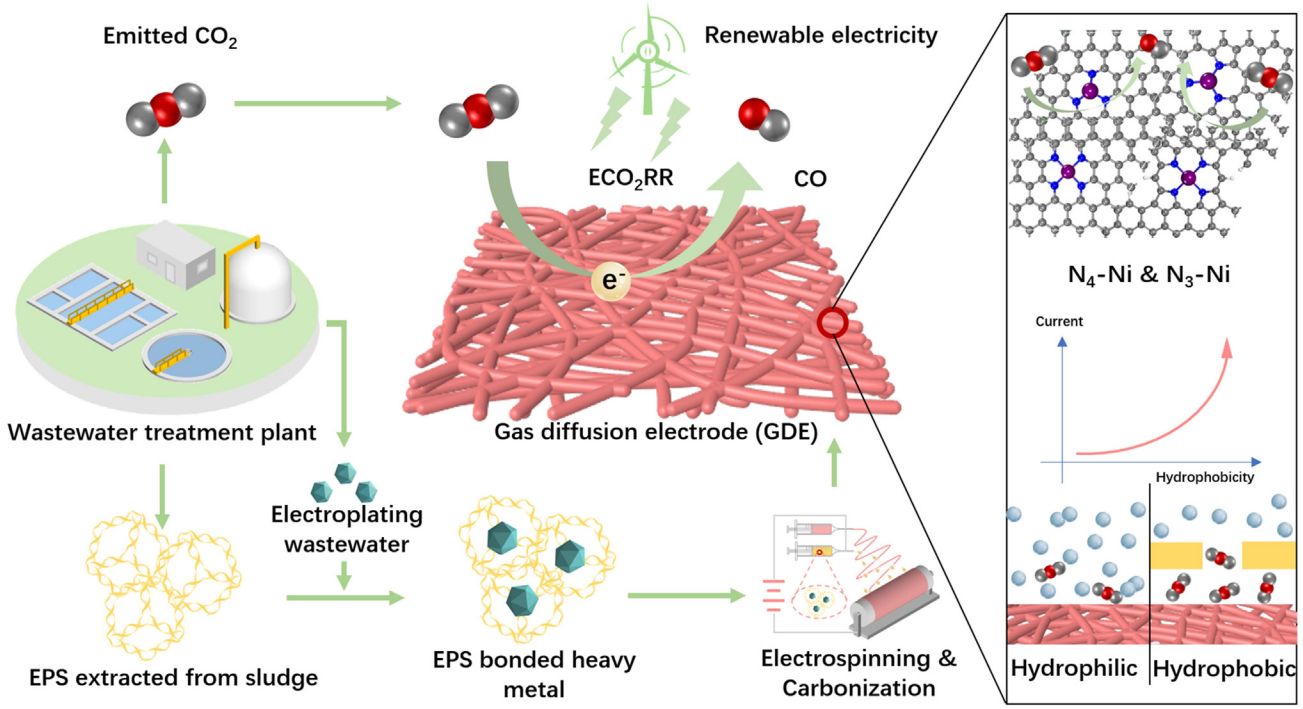

Figure 1. Schematic of co-utilization of wastewater sludge EPS and heavy metal to deliver electrochemical CO_2 conversion

desorption of CO (CO*).[20] In contrast, the prevailing carbon matrices (e.g., CNTs, MOFs, COFs, and etc.) for N_x-Ni formation are costly, developing the cheap and N-enriched alternatives are necessary. The WAS-derived EPS has plentiful N-contained functional groups, which can provide essential N element for N_x-Ni formation during carbonization. So far, the use of N-rich wastes for SACs preparation is rarely reported.

In this study, we originally used WAS-derived EPS to capture Ni in the real wastewater and directly converted the EPS-Ni ligands into a Ni-SAs distributed gas diffusion electrode (GDE) through electrospinning coupled with carbonization (Figure 1). This novel strategy integrates both catalyst synthesis and electrode fabrication, thus simplifying the GDE manufacture process for cost reduction. Currently matured electrospinning technique allows to fabricate large-scale GDE with increased exposure of catalytic sites on the GDE nanofibers. The as-prepared GDE with hydrophobic treatment could be applied in the membrane electrode assembly (MEA) for direct gaseous CO_2 reduction into CO (Figures 1 and S1). This configuration significantly suppresses the preferred H_2 evolution in conventional liquid-phase CO_2 reduction, and demonstrates the enhanced ECO_2RR kinetics due to a higher CO_2 diffusion coefficient (16 $mm^2 \cdot s^{-1}$) in gaseous-phase (vs. 0.0016 $mm^2 \cdot s^{-1}$ in liquid-phase)[21,22] and the low electrochemical resistance resulted from the sandwiched configuration of MEA (Figure S1). The roles of individual EPS compositions (protein, polysaccharide, and humic acid) in the SACs formation and the corresponding ECO_2RR performance and catalytic mechanisms were investigated. The results show the excellent CO selectivity (~75% FE_{CO} and CO:H_2 ratio of ~100) with large current density of 50 $mA \cdot cm^{-1}$ and the great potential for win-win on both resource recovery and environment remediation in large-scale.

RESULTS

Characterization of gas diffusion configuration of GDE_{EPS}

The as-formed gas diffusion configuration of GDE_{EPS} allows gaseous CO_2 to diffuse into the electrode inside for direct electrochemical reduction between the liquid and the gaseous phase. This conjunction of solid/liquid/gas interface enables to suppress competitive H_2 evolution reaction at a conventional solid/liquid interface.[21–24] Electrospinning method employed here is able to fabricate large-size GDE_{EPS} with ~200 cm^2 (Figure S3), and its size can be further enlarged by using industrial-scale instrument. For the microscopic structure, electrospinning enables disordered stack of numerous fibers with diameter of ~300 nm (Figures 2A, 2B, and S4). Millimetric fractures spreading on the hydrophobic PTFE layer provides ample region for gas crossing since the dynamic diameter of CO_2 is merely 3.4 Å (Figures 2C and 2D).[20] The ~300-μm thick GDE_{EPS} is full of cavities with various dimensions below the PTFE layer, capable of gas and liquid diffusion (Figures 2E and 2F). Exposure of ample Ni catalysts on the nanofibers' surface facilitates more contact between catalytic sites and CO_2 molecules (Figure 2G). BET result shows that GDE_{EPS} is capable of CO_2 storage with ~8 cm^3-$CO_2 \cdot g^{-1}$-GDE_{EPS} under atmospheric pressure (Figure 2H). Type IV N_2 ad-desorption isotherm with meso-macropores distribution demonstrates well developed channels for gas diffusion.[17] The incremental pore volume mainly located between 50 and 250 nm further proves this opinion (Figures 2H–2J and S5). One side of GDE_{EPS} was coated by one layer of PTFE with a contact angle of 112.19° (Figures 2K and S6). In an electrolyte penetration test using fluorescent dye, confocal laser scanning microscope detects a penetration depth of only a few micrometers for GDE_{EPS} with PTFE layer, in contrast, the counterpart without

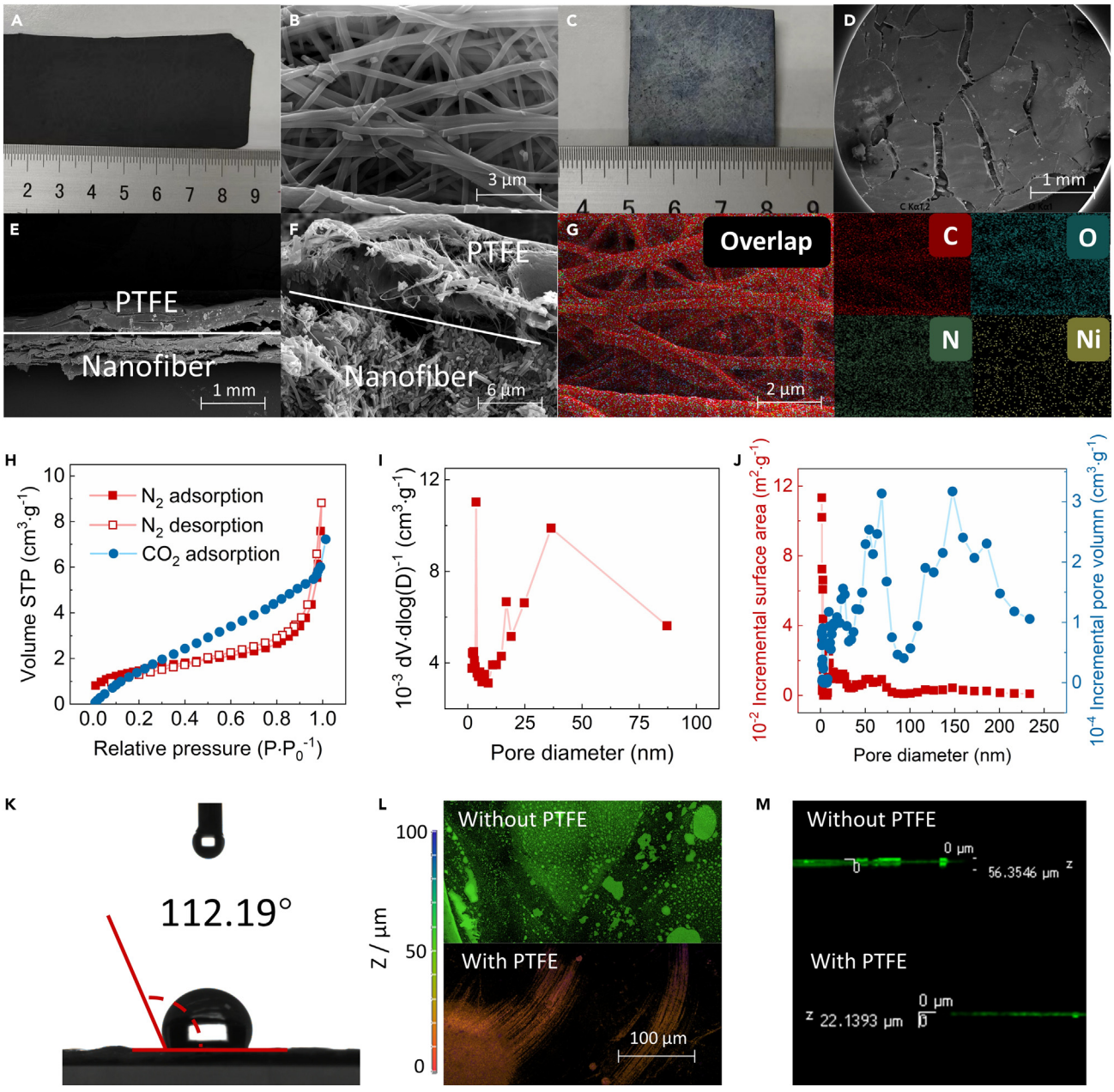

Figure 2. Gas diffusional configuration of GDE_{EPS}

Photographs and SEM images of GDE_{EPS} surface without PTFE layer (A and B) and with PTFE layer (C and D).

(E and F) SEM images of cross section of GDE_{EPS}.

(G) Elemental mapping of GDE_{EPS} surface.

(H–J) BET analysis.

(K) Contact angle of GDE_{EPS} at PTFE layer.

(L and M) Confocal laser scanning microscope images of overlapped plane and cross section of GED_{EPS} wetted by dye (1 M KOH/NaOH solution containing Rhodamine B) to show the penetration level on GED_{EPS} surface by water. The color represents the different penetration depth in l, and the thickness of green stripe indicates the penetration depth in m.

PTFE layer was penetrated considerably with more than 50 μm depth (Figures 2L, 2M, and S7). These results indicate that the well hydrophobicity was provided by a PTFE layer.

The distribution of catalytic sites onto GDE_{EPS} (poised at −0.6 V vs. RHE) surface was detected by a scanning electrochemical microscopy equipped with a Pt ultramicroelectrode tip (poised at 0.84 V vs. RHE) that move across GDE_{EPS} surface to oxidizes the ECO_2RR products of CO

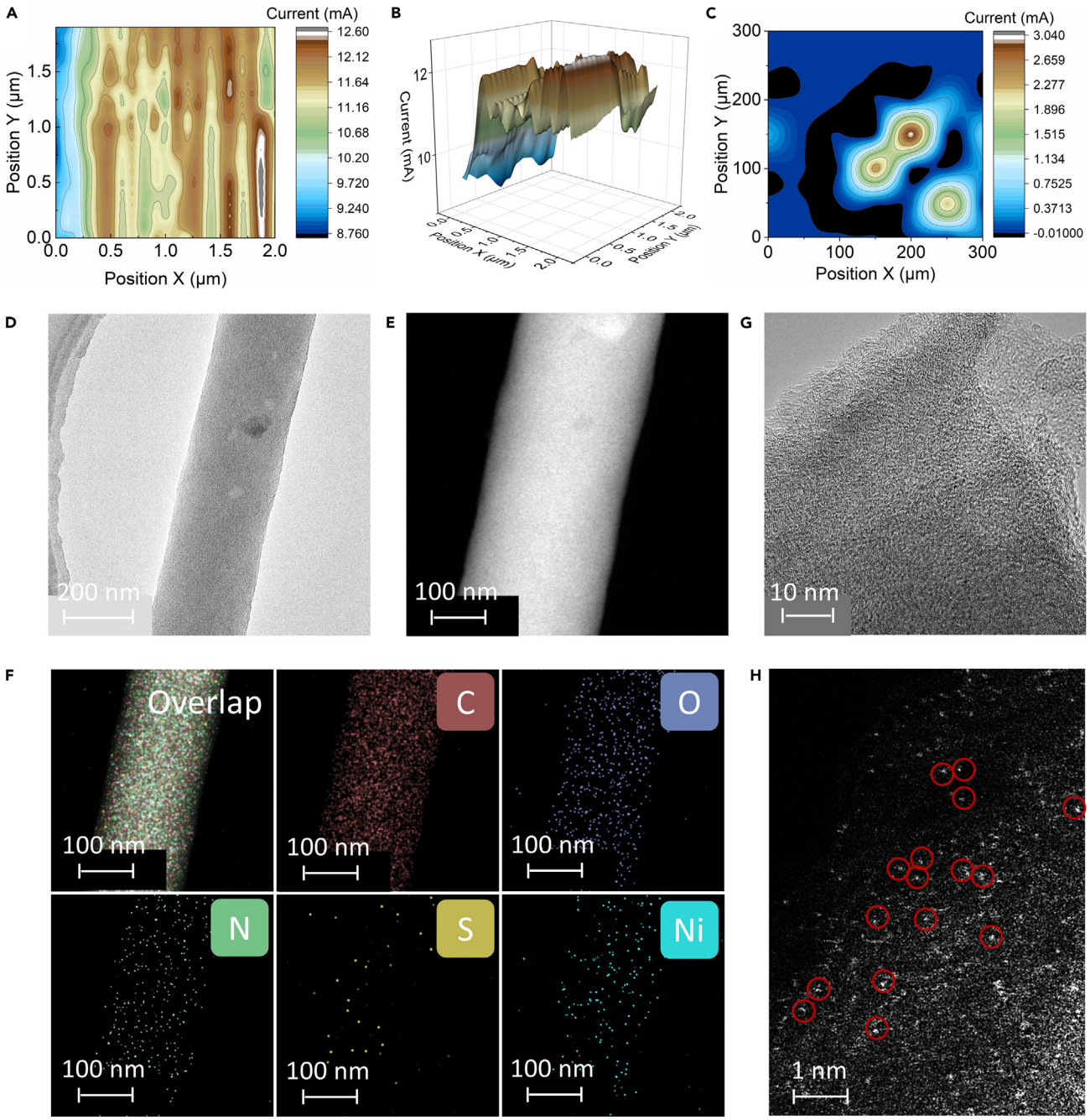

Figure 3. Characterization of Ni SACs dispersed on the nanofibers of GDE_{EPS}

Current signal images collected by a scanning electrochemical microscopy for (A and B) the microscopic structure of GDE_{EPS} (plane or 3D contour charts) and (C) a whole GDE_{EPS} (bright part) fixed by epoxy resin (dark part) with scanning step length of 50~100 nm·s^{-1}.

(D–F) TEM and HAADF-STEM images of a single nanofiber of GDE_{EPS}.

(G) Marginal TEM image of nanofiber with clear graphene-liked lattice.

(H) Aberration-corrected HAADF-STEM image of Ni single atoms that are highlighted by red cycles.

or H_2 to generate the current, which allows to image electrochemical activity (Figures 3A–3C and S8). The overall current distribution just like a wave with the waviness width of 200–300 nm (Figures 3A and 3B), consistent with the diameter of GDE_{EPS} nanofibers, indicating that efficient catalytic sites are well located at each fiber's surface. As a comparison, the surface of epoxy resin used to fix GDE_{EPS} presents ~0 current signals and a clear boundary formed between GDE_{EPS} and epoxy resin (Figure 3C). Upon the nanometer and even atomic view, Ni SAs

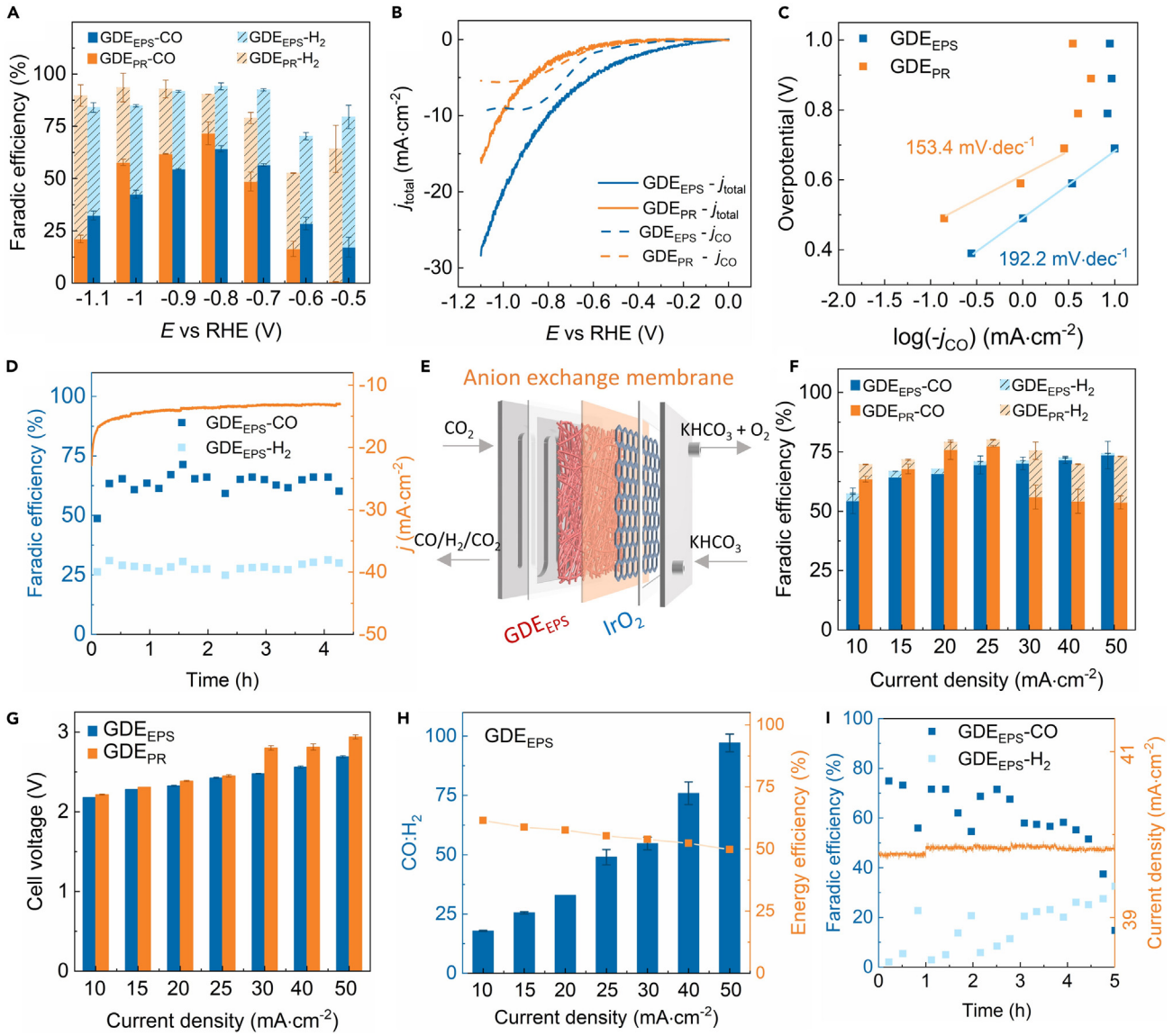

Figure 4. Performance of GDE$_{EPS}$ for ECO$_2$RR

(A) Faradic efficiency (FE) for CO and H_2 production, (B) corresponding current density and (C) Tafel plots under different potentials as well as (D) long-term stability of GDE$_{EPS}$ (−0.8 V vs. RHE) that were tested in bulk solution using a single-chamber three-electrode electrochemical cell. The GDE$_{EPS}$ was also tested in a (E) MEA for examining (F) CO and H_2 selectivity, (G) cell voltage of MEA, (H) a molar ratio of CO to H_2 produced and the energy efficiency under different current densities as well as (I) long-term stability of GDE$_{EPS}$ under 40 mA·cm^{-2} operation. A GDE$_{PR}$ fabricated by using pure protein as matrix is served as a control. Data are reported as average ±SD.

are well dispersed onto the surface of nanofibers and surrounded by quantitative N element (Figure 3D–3H). No Ni nanoparticles are detected, indicating protein-rich EPS may prevent the Ni agglomeration. In contrast, we found that the Ni nanoparticles formed on the GDEs that were made by using polysaccharide and humic acid as matrix. Because the powders obtained by milling these GDEs were attracted by a neodymium magnet (Figure S9), which is an indicator of metal particles formed. This observation indicates the incapability of N-poor matrix to disperse or anchor Ni SAs. Interestingly, a GDE without matrix (manufacture by only N-contained supporting material of PAN) shows formation of both abundant Ni SAs and a few of Ni nanoparticles on the fibers (Figures S9–S12). This further approves the importance of N-doping for forming Ni SAs, and the introduction of N-poor matrixes may be detrimental to this process.

Performance of GDE$_{EPS}$ for ECO$_2$RR

The performance of GDE$_{EPS}$ for ECO$_2$RR was tested in both bulk solution and a MEA (Figure 4). GC results reveal that H_2 and CO are only gaseous products, while H^1 NMR spectra does not identify the production of organic compounds in liquid (Figure S13). In the bulk solution,

the Faradic efficiency of CO production (FE_{CO}) by GDE_{EPS} reaches a maximum of 64.3% (−0.8 V vs. RHE, 9.96 $mA \cdot cm^{-2}$), which is comparable with ∼71.8% of GDE_{PR} (2.82 $mA \cdot cm^{-2}$) fabricated by using pure protein, the main composition in EPS, as matrix (Figures 4A and 4B). The higher current obtained by GDE_{EPS} can be attributed to its larger conductivity. The fundamental single-electron transfer dominates the rate-limiting step with a Tafel slope of 192.2 $mV \cdot dec^{-1}$ (Figure 4C). Applying GDE_{EPS} as the cathode in the MEA (Figure 4E), the CO selectivity is remained even under the higher current density (∼50 $mA \cdot cm^{-2}$). H_2 evolution is significantly suppressed (FE_{H2} ∼5%) due to the lack of H_2O surrounding the cathode (Figure 4F). A molar ratio of CO to H_2 in MEA (∼100) is far higher than that obtained in bulk solution using a single-chamber cell (∼2.5) (Figures 4H and S14). However, the total Faradic efficiency of MEA (∼75%) is lower than that in bulk solution (∼95%), which could be attributed to the redox reaction occurred on the GDE material to consume the electron. The energy efficiency of MEA for CO production is around 50%–60% with a cell voltage between 2 V and 3 V (Figures 4G and 4H). Long-term operation under high current density of ∼40 $mA \cdot cm^{-2}$ demonstrates the durability of GDE_{EPS} (Figures 4D and 4I). The GDE_{PR} fabricated by the pure protein shows the similar performance as the GDE_{EPS} in MEA (Figures 4 and S15). The thickness of the GDE plate on the electrocatalytic performance was also tested using 2 plates in 1 mm and 0.5 mm thickness, respectively. The 1 mm-thick plate was the employed GDE in this study, while the 0.5 mm-thick plate was sliced from the 1 mm-thick plate. However, the thickness seemed to show limited effect on CO evolution at the same potential window (Figure S16). Furthermore, the carbonization temperature of 800°C–1000°C also exerted limited effect on CO evolution (Figure S17), demonstrating that lower energy input can also prepare GDE with similar electrocatalytic performance.

The role of different organic compositions of EPS in CO_2 reduction

The role of different organic compositions of EPS in ECO_2RR was further investigated by using these compositions as matrixes to fabricate the ECO_2RR catalysts (Figure 5). The onset potential of CO production by EPS-based catalyst is −0.4 V (vs. RHE), indicating that the overpotential is at least smaller than 0.29 V since the theoretical potential of CO_2 to CO conversion is −0.11 V (Figure 5A). The CO selectivity (FE_{CO}) reaches the maximum of 50.2% at the potential between −0.7 V and −0.8 V, further applying the more negative potential will decrease the FE_{CO}. Protein-based catalyst presents the highest FE_{CO} of ∼92.0% at −0.8 V vs. RHE (Figures 5A and S18). The polysaccharide and humic acid-based catalysts as well as the supporting material of PAN are more liable to produce H_2 over CO. Protein has abundant N-contained functional groups other than dominant C-contained functional groups existed in the polysaccharide and humic acid.[14,16] Our results and many previous studies show that the N-doping is crucial in CO_2 reduction to CO,[3,5,19,25] since N-doping favors the formation of Ni SAs (Figure 2D–2H) and N_x-Ni coordination that presents relatively weak binding energy for CO*, an important intermediate during ECO_2RR, and thus facilitates CO evolution.[8,19] In contrast, polysaccharide and humic acid-based catalysts as well as PAN with a little N-doping tend to form Ni particles (Figure S9), which are regarded as desirable catalysts for H_2 evolution. This was also supported by an observation that FE_{CO} obviously increased after acid soaking of these catalysts to exclude Ni particles (Figure S10). Moreover, the control of catalyst fabricated by polysaccharide + PVA with no N-doping shows the lowest CO selectivity regardless of whether acid soaking, indicating the importance of N-doping. The difference in matrix also affects the current density of the catalysts (Figure 5B), which is consistent with GDE performance (Figure 4B).

Tafel slopes partly explain reasons for the difference of CO selectivity. EPS, protein and PAN-based catalysts show the slopes of 187–198 $mV \cdot dec^{-1}$ under the low overpotential window, indicating the capability to conduct CO_2 reduction in this range (Figures 5C and S19).[8] Humic acid and polysaccharide-based catalysts demonstrate the ultrahigh or even negative slope at the whole overpotential window, suggesting inactivity of catalytic sites for ECO_2RR. Therefore, extremely low turnover frequencies (TOF) (<10 h^{-1}, calculations were provided in SI) were observed for the polysaccharide and humic acid-based catalysts. Electrochemical double layer capacity, an indicator of the electrochemical structure, was used to calculate the TOF. However, no correlation between electrochemical double layer capacity and CO TOFs was observed (Figures 5D and 5E), indicating that other factors (e.g., the number of efficient catalytic sites, specific areas etc.) rather than electrochemical structure have more influence on CO_2 to CO conversion. The presence of small amounts of polysaccharide and humic acid (∼10 wt %) in EPS-based catalyst (∼90 wt % protein) (Table S2) is also detrimental to the CO evolution compared to the protein-based catalyst (Figure 5A) despite few Ni nanoparticles were detected in both catalysts, suggesting that these impurities (polysaccharide and humic acid) may impair the formation of efficient catalytic sites.

The significance of N_x-Ni formation on CO_2 reduction

The mass loading of Ni was below 1 at% in all catalysts (Figure S20). There is no obvious Ni crystal peak observed in the X-ray photoelectron spectroscopy (XPS) with no obvious peak of zero-valent Ni (852.6 eV) detected (Figure 6A), indicating these catalysts are capable of well dispersing Ni SAs. A peak between the 852.6 eV (zero-valent Ni) and 855.8 eV (entirely oxidized Ni) is observed, which represents partially oxidized Ni for Ni SAs.[5,8,20] For catalyst without any N-doping (polysaccharide + PVA), the visible peak of zero-valent Ni shows it is much more liable to form Ni particles (Figures 6A, S20, and S21). N_x-Ni structure has been proved to be crucial for CO_2 to CO conversion.[16,17,25] The higher proportion of N_x-Ni in the N 1s spectra was observed in EPS, protein and PAN-based catalysts, indicating numerous catalytic sites for CO_2 to CO conversion in these catalysts (Figure 6B). The N-contained functional groups in these catalysts may provide N element for the formation of N_x-Ni. The obvious change in the N 1s spectra after Ni loading was observed for protein (3.49 at% N element) (Table S4; Figure S22), indicating that N-contained functional groups in protein participate in Ni anchoring. Interestingly, there is a negligible change in the N 1s spectra but an obvious change in C 1s and O 1s spectra after Ni loading by EPS (14.26 at% N element), suggesting the C- and O-contained functional groups in EPS are more competitive than N-contained functional groups in seizing Ni. The Ni species in EPS- and protein-based catalysts show the higher valence than Ni^{2+} (NiO and NiPc) and Ni^0 (Ni foil) due to their higher energy location than Ni^{2+} and Ni^0 in X-ray absorption near-edge spectroscopy (XANES) and 1st derivation XANES spectra (Figures 6C and 6D). EPR results present

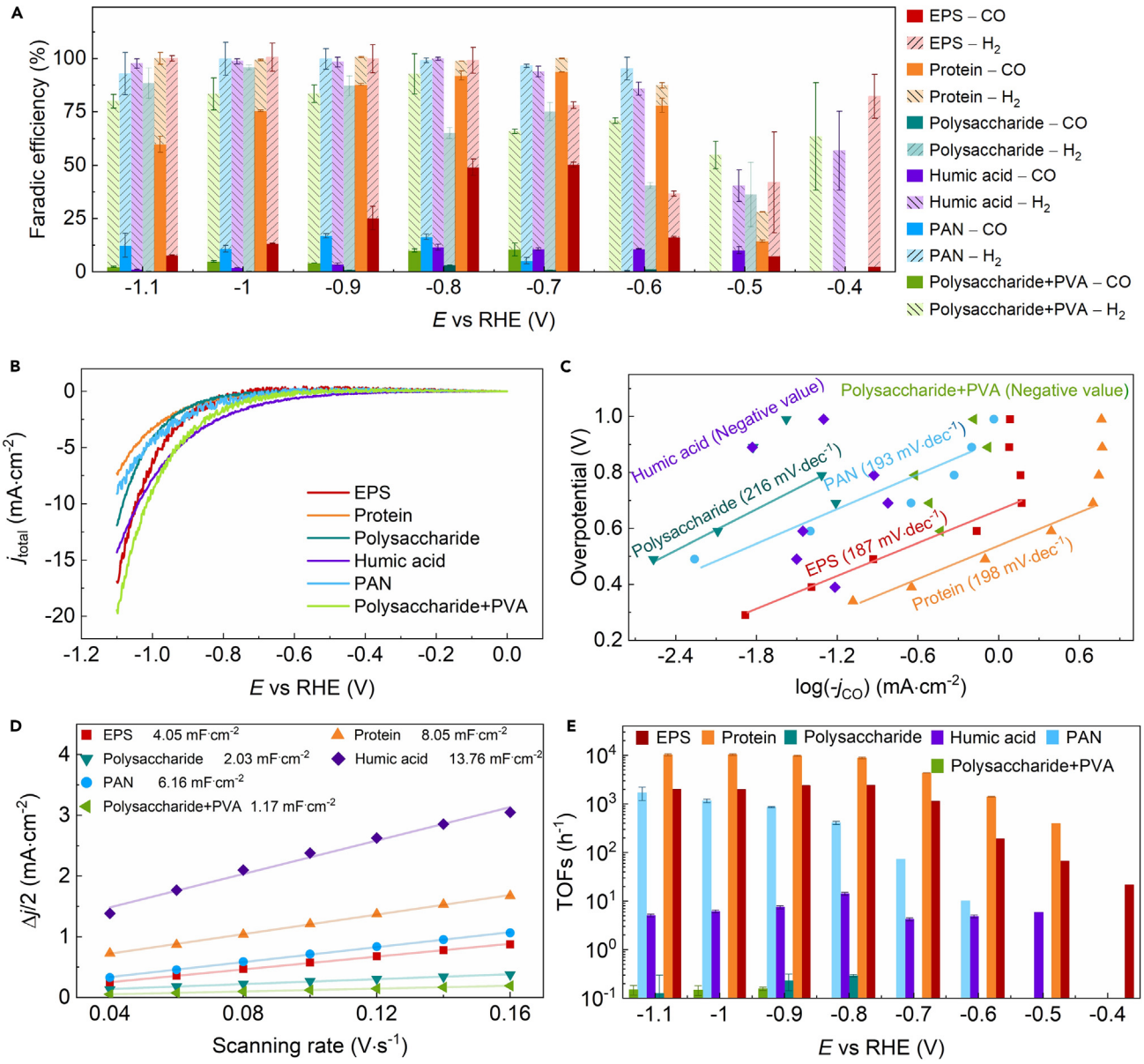

Figure 5. The role of different organic compositions of EPS in ECO_2RR

(A) CO and H_2 selectivity, (B) current density, (C) Tafel plots, (D) electrochemical double layer capacitance, and (E) turnover frequency (TOF) of different ECO_2RR catalysts fabricated by using different compositions of EPS as matrixes. The catalytic experiments were conduct in bulk solution using a single-chamber three-electrode electrochemical cell. Data are reported as average ±SD.

a signal at 150–450 mT for both EPS- and protein-based catalysts, which also indicates the existence of high-valence Ni species in these catalysts (Figure 6E), and it was like +3 valent compared with studies of Zhecheva et al.[26] However, EPS-based catalyst displays a slight shift toward lower energy, indicating its Ni species have a lower valence than protein-based catalyst.[24,25]

Fourier transformed (FT) k^2-weighted extended X-ray absorption fine structure (FT-EXAFS) spectra (Figures 6F, 6G, and S23) and wavelet transform (WT) of χ(k) spectra (Figure 6H) clearly demonstrate N-Ni coordination over Ni-O or Ni-Ni coordination in EPS- and protein-based catalysts. A coordination number of 3.6 ± 0.3 suggests the presence of both N_3-Ni and N_4-Ni in EPS-based catalyst while the N_4-Ni is dominant in protein-based catalyst with a coordination number of 4.1 ± 0.2 (Table S6). Because the both pyridinic N and pyrrolic N were found in XPS splitting spectra, we propose the existence of 4 kinds of N_x-Ni structures, namely pyrrolic N_3-Ni and N_4-Ni as well as pyridinic N_3-Ni and N_4-Ni, based on the results of XPS and EXFAS (Figure 6I). The results show that pyrrolic N_4-Ni must exist in a coordination with some vacancies, which is different from pyrrolic N_3-Ni and pyridinic N_3-Ni/N_4-Ni where vacancy is not necessary in the coordination. This is consistent with the previous finding that Ni is distinct than Fe, Co, Cu, Mn and etc. whose pyrrolic N_4-metal coordination could exist without any

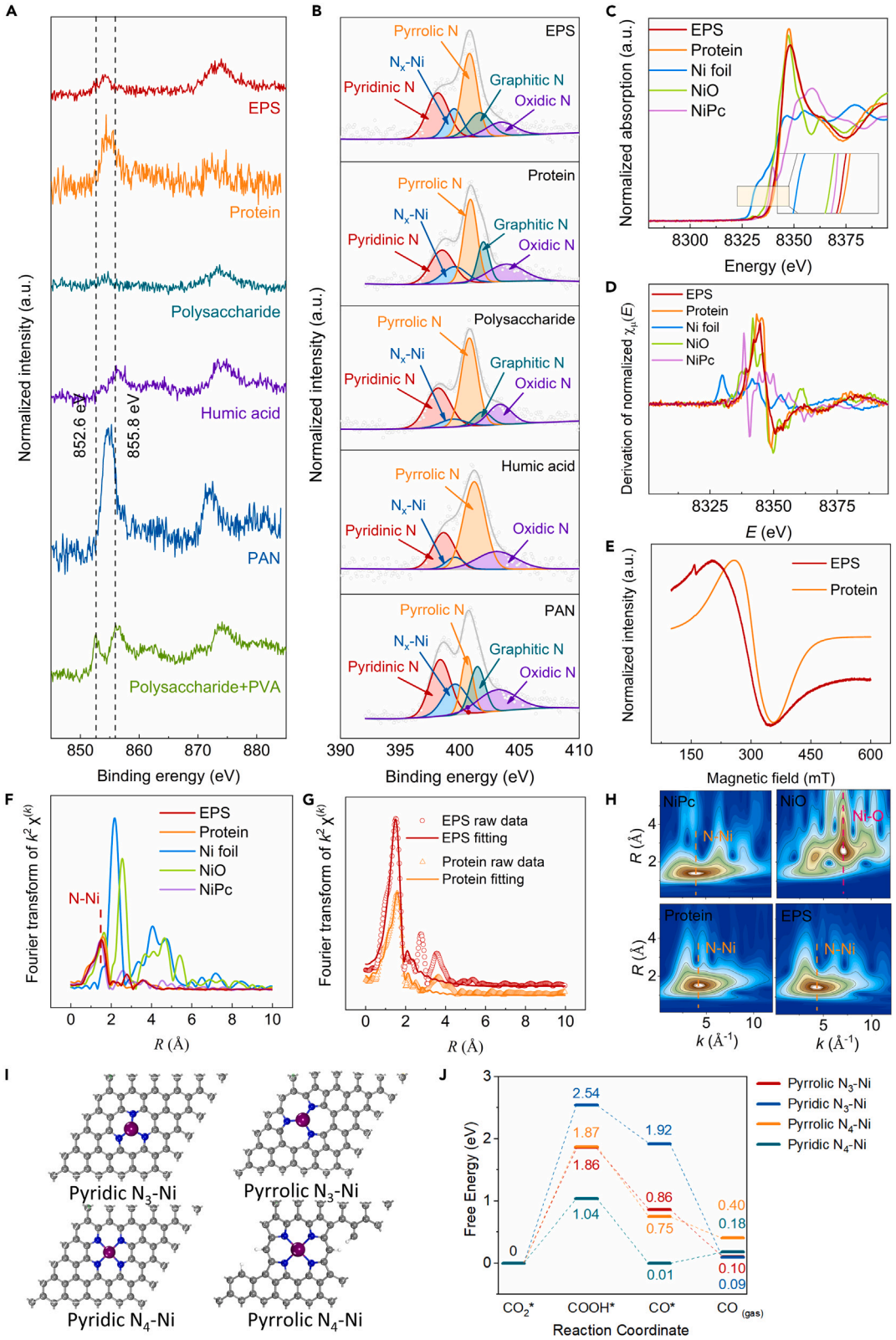
A
EPS
Protein
Polysaccharide
Humic acid
PAN
Polysaccharide+PVA
852.6 eV
855.8 eV
Normalized intensity (a.u.)
Binding erengy (eV)
B
Pyrrolic N
N$_x$-Ni
Pyridinic N
Graphitic N
Oxidic N
EPS
Protein
Polysaccharide
Humic acid
PAN
Normalized intensity (a.u.)
Binding energy (eV)
C
EPS
Protein
Ni foil
NiO
NiPc
Normalized absorption (a.u.)
Energy (eV)
D
Derivation of normalized $\chi_\mu(E)$
E (eV)
E
Normalized intensity (a.u.)
Magnetic field (mT)
F
Fourier transform of $k^2\chi^{(k)}$
N-Ni
R (Å)
G
EPS raw data
EPS fitting
Protein raw data
Protein fitting
H
NiPc
NiO
Ni-O
Protein
EPS
R (Å)
k (Å^{-1})
I
Pyridic N$_3$-Ni
Pyrrolic N$_3$-Ni
Pyridic N$_4$-Ni
Pyrrolic N$_4$-Ni
J
Pyrrolic N$_3$-Ni
Pyridic N$_3$-Ni
Pyrrolic N$_4$-Ni
Pyridic N$_4$-Ni
Free Energy (eV)
2.54
1.87
1.86
1.92
1.04
0.86
0.75
0.40
0.18
0.10
0.09
0.01
0
CO$_2$*
COOH*
CO*
CO (gas)
Reaction Coordinate

Figure 6. Characterizations of chemical bonds in different ECO_2RR catalysts fabricated by using different compositions of EPS as matrixes

(A) XPS spectra of Ni 2p, (B) XPS spectra of N 1s splitting peaks, (C) XANES spectra at the Ni K-edge, (D) the first derivate of XANES spectra, (E) EPR results, (F and G) the Fourier transform of EXAFS, (H) Wavelet transform (WT) of $\chi(k)$ spectrum, and (I and J) proposed 4 N_x-Ni structures and corresponding Gibbs free energy change during CO_2 to CO conversion.

vacancy.[27,28] Generally, the N_4-Ni coordination requires relatively lower energy for ECO_2RR than N_3-Ni regardless of pyridinic or pyrrolic N coordination (Figures 6K and S24). This explains that why protein-based catalyst (N_4-Ni coordination) presents better ECO_2RR performance than EPS-based catalyst (mixture of N_4-Ni and N_3-Ni coordination). In other hand, the existence of polysaccharide and humic acid will prevent the formation of N_4-Ni to lead to the poor ECO_2RR performance.

DISCUSSION

We extracted EPS from wastewater sludge to adsorb the Ni in electroplating wastewater, and the EPS-Ni mixture was then electrospun into an integrated GDE for the electro-conversion of CO_2 to CO. This strategy enabled the Ni dispersed onto the nanofiber's surface of the GDE in an atomic form, which delivered the desirable CO_2 conversion with >60% FE_{CO}. The protein over polysaccharide and humic acid in the EPS was found as the foremost matrix to synthesize efficient catalyzing sites, as the N-enriched functional groups in protein provided quantitative N element for the formation of N_X-Ni. The further analysis pointed that the mixture of N_3-Ni/N_4-Ni played the big role in CO_2 conversion, and the pyridinic N_4-Ni portfolio was more preferable. Scaling up the current density and directly inserted the GDE into a MEA, the swift conversion of CO_2 to CO was also delivered with ~75% FE_{CO} under 2.69 V cell voltage.

Annually, a huge amount of WAS is produced globally, leading to the great environmental risk and GHG emission. For example, around ~30.8 million tons of sludge (dry weight) is produced in major economies, meaning that ~15.4 million tons of EPS could be reclaimed given ~50 wt % recovery ratio.[2,29–31] The medium C and N content in dry biomass are estimated to 31.39 wt % and 3.97 wt %,[30] equaling to 4.83 million tons C and 0.61 million tons N. The scenario of *in situ* CO_2 reduction in wastewater treatment plant can be divided into 4 steps, including the CO_2 feed, electrocatalytic process (both GDE manufacture and electrocatalysis), electrical energy input, and product separation (Figure S25). Herein, we assume that a direct feed of anaerobic digestion biogas (30–40% CO_2) to the electrocatalytic process, without CO_2 capture procedure, will be conducted as well as a high Faradic efficiency (FE) for CO and H_2 production will be obtained (experiment shows an approximate 100% FE), thus the associated carbon-foot and cost derived from steps of CO_2 feed and product separation are excluded from the calculation. The analysis shows that a total of 0.67-ton CO_2 will be mitigated by generating one ton CO, with the consideration of CO_2 fixation in the GDE manufacture, CO_2 to CO conversion by electrocatalysis, and indirect CO_2 emission due to electricity consumption. A net profit of US$1809 per ton CO-produced will be obtained by including the CO global market, CO production cost and the revenues due to wastes recovery and H_2 production (Detailed calculation was provided in Text S3).

Given that protein plays an important role in CO selectivity, other protein-rich wastes, such as soybean peptide and albumen wastes generated from food industry, have also been investigated for synthesizing the corresponding GDEs (labeled as GDE_{SP} and GDE_{AL}), presenting similar CO selectivity as GDE_{EPS} (Figures S26 and S27). This shows a great potential for more CO_2-CO conversion by using various N-rich wastes. This route can also be directly integrated with an anaerobic fermentation, where the target products of CO_2 reduction will be switched to 1C organics (e.g., formate and methanol) that subsequently return to the fermenter for *in situ* improving methanogenesis.

Limitations of the study

Although the GDE_{EPS} fabricated here shows characteristics of low-cost, sustainability, and the efficient CO_2 to CO conversion, two major challenges need to be resolved in future. The first is the inferior conductivity of GDE_{EPS} compared with traditional CNTs, MOFs, and etc., which limits the current density in the MEA configuration. High current density (>200 $mA \cdot cm^{-2}$) is the threshold for the profit competing with other CO_2 conversion technologies. The second is the durability needed to be further extended. Despite the GDE_{EPS} is relatively stable under high current density operation, there is still a gap between the performance and the practical scenario. Further surface modification of GDE_{EPS} to simultaneously improve the conductivity and stability is the key to promote the application of GDE_{EPS} for CO_2-CO conversion.

STAR★METHODS

Detailed methods are provided in the online version of this paper and include the following:

- KEY RESOURCES TABLE
- RESOURCE AVAILABILITY
  - Lead contact
  - Materials availability
  - Data and code availability
- EXPERIMENTAL MODEL AND STUDY PARTICIPANT DETAILS
- METHOD DETAILS
  - EPS extraction from sludge
  - Treatment of the Ni-contained electroplating wastewater
  - GDE fabrication based on electrospinning

- PTFE layer preparation
- ECO_2RR experiment
- GDE characterizations
- Measurement of protein, polysaccharide and humic acid content in EPS
- Calculations
- Evaluation of turnover frequency (TOF)
- Calculation of potential carbon-foot and economic benefits in practice

- QUANTIFICATION AND STATISTICAL ANALYSIS

SUPPLEMENTAL INFORMATION

Supplemental information can be found online at https://doi.org/10.1016/j.isci.2024.109956.

ACKNOWLEDGMENTS

This work was financially supported by the National Natural Science Foundation of China (22176046), Science Fund for Creative Research Groups of the National Natural Science Foundation of China (52321005), Shenzhen Science and Technology Program (KQTD20190929172630447, JCYJ20210324124209025 and GXWD20220811173949005), and Natural Science Foundation of Guangdong Province (2022A1515012016).

AUTHOR CONTRIBUTIONS

B.Z. and L.L. conceived the experiments and wrote the manuscript. B.Z. did the material fabrication and characterizations as well as electrochemical measurement. Z.L., X.H., and C.Z. did material and electrochemical characterizations. S.P., M.Y., G.L., and Z.Z. prepared matrix for GDE synthesis. W.Z. provided insightful clues in designing the MEA. There is no competing interest within the authors.

DECLARATION OF INTERESTS

L.L., B.Z., Z.L., and C.Z. are co-inventors on filed China patent ZL202210841460.1 related to a method for GDE fabrication based on electrospinning technology that incorporate discoveries included in this manuscript.

Received: March 7, 2024
Revised: April 9, 2024
Accepted: May 8, 2024
Published: May 10, 2024

REFERENCES

1. Lu, L., Guest, J.S., Peters, C.A., Zhu, X., Rau, G.H., and Ren, Z.J. (2018). Wastewater treatment for carbon capture and utilization. Nat. Sustain. *1*, 750–758. https://doi.org/10.1038/s41893-018-0187-9.
2. Drechsel, P., Qadir, M., and Wichelns, D. (2015). Wastewater, Economic Asset in the Urbanizing World (Springer). https://doi.org/10.1007/978-94-017-9545-6_1.
3. Zheng, T., Jiang, K., Ta, N., Hu, Y., Zeng, J., Liu, J., and Wang, H. (2019). Large-Scale and Highly Selective CO_2 Electrocatalytic Reduction on Nickel Single-Atom Catalyst. Joule *3*, 265–278. https://doi.org/10.1016/j.joule.2018.10.015.
4. Liu, C., Wu, Y., Sun, K., Fang, J., Huang, A., Pan, Y., Cheong, W.C., Zhuang, Z., Zhuang, Z., Yuan, Q., et al. (2021). Constructing FeN_4/graphitic nitrogen atomic interface for high-efficiency electrochemical CO_2 reduction over a broad potential window. Chem *7*, 1297–1307. https://doi.org/10.1016/j.chempr.2021.02.001.
5. Jiang, K., Siahrostami, S., Zheng, T., Hu, Y., Hwang, S., Stavitski, E., Peng, Y., Dynes, J., Gangisetty, M., Su, D., et al. (2018). Isolated Ni single atoms in graphene nanosheets for high-performance CO_2 reduction. Energy Environ. Sci. *11*, 893–903. https://doi.org/10.1039/C7EE03245E.
6. Tripkovic, V., Vanin, M., Karamad, M., Björketun, M.E., Jacobsen, K.W., Thygesen, K.S., and Rossmeisl, J. (2013). Electrochemical CO_2 and CO Reduction on Metal-Functionalized Porphyrin-like Graphene. J. Phys. Chem. C *117*, 9187–9195. https://doi.org/10.1021/jp306172k.
7. Peterson, A.A., and Nørskov, J.K. (2012). Activity Descriptors for CO_2 Electroreduction to Methane on Transition-Metal Catalysts. J. Phys. Chem. Lett. *3*, 251–258. https://doi.org/10.1021/jz201461p.
8. Yang, H.B., Hung, S.F., Liu, S., Yuan, K., Miao, S., Zhang, L., Huang, X., Wang, H.Y., Cai, W., Chen, R., et al. (2018). Atomically dispersed Ni(i) as the active site for electrochemical CO_2 reduction. Nat. Energy *3*, 140–147. https://doi.org/10.1038/s41560-017-0078-8.
9. Krause, R., Reinisch, D., Reller, C., Eckert, H., Hartmann, D., Taroata, D., Wiesner-Fleischer, K., Bulan, A., Lueken, A., and Schmid, G. (2020). Industrial Application Aspects of the Electrochemical Reduction of CO_2 to CO in Aqueous Electrolyte. Chem. Ing. Tech. *92*, 53–61. https://doi.org/10.1002/cite.201900092.
10. Masel, R.I., Liu, Z., Yang, H., Kaczur, J.J., Carrillo, D., Ren, S., Salvatore, D., and Berlinguette, C.P. (2021). An industrial perspective on catalysts for low-temperature CO_2 electrolysis. Nat. Nanotechnol. *16*, 118–128. https://doi.org/10.1038/s41565-020-00823-x.
11. Verma, S., Kim, B., Jhong, H.R.M., Ma, S., and Kenis, P.J.A. (2016). A gross-margin model for defining technoeconomic benchmarks in the electroreduction of CO_2. ChemSusChem *9*, 1972–1979. https://doi.org/10.1002/cssc.201600394.
12. Cui, P., Liu, C., Su, X., Yang, Q., Ge, L., Huang, M., Dang, F., Wu, T., and Wang, Y. (2022). Atomically Dispersed Manganese on Biochar Derived from a Hyperaccumulator for Photocatalysis in Organic Pollution Remediation. Environ. Sci. Technol. *56*, 8034–8042. https://doi.org/10.1021/acs.est.2c00992.
13. Hao, X., An, X., Patil, A.M., Wang, P., Ma, X., Du, X., Hao, X., Abudula, A., and Guan, G. (2021). Biomass-Derived N-Doped Carbon for Efficient Electrocatalytic CO_2 Reduction to CO and Zn−CO_2 Batteries. ACS Appl. Mater. Interfaces *13*, 3738–3747. https://doi.org/10.1021/acsami.0c13440.
14. Yu, H.Q. (2020). Molecular Insights into Extracellular Polymeric Substances in Activated Sludge. Environ. Sci. Technol. *54*, 7742–7750. https://doi.org/10.1021/acs.est.0c00850.

15. Ajao, V., Nam, K., Chatzopoulos, P., Spruijt, E., Bruning, H., Rijnaarts, H., and Temmink, H. (2020). Regeneration and reuse of microbial extracellular polymers immobilised on a bed column for heavy metal recovery. Water Res. *171*, 115472. https://doi.org/10.1016/j.watres.2020.115472.
16. Sheng, G.P., Xu, J., Luo, H.W., Li, W., Li, W., Li, W.W., Xie, Z., Li, W.H., and Hu, F.C. (2013). Thermodynamic analysis on the binding of heavy metals onto extracellular polymeric substances (EPS) of activated sludge. Water Res. *47*, 607–614. https://doi.org/10.1016/j.watres.2012.10.037.
17. Mikutta, R., Baumgärtner, A., Schippers, A., Haumaier, L., and Guggenberger, G. (2012). Extracellular Polymeric Substances from Bacillus subtilis Associated with Minerals Modify the Extent and Rate of Heavy Metal Sorption. Environ. Sci. Technol. *46*, 3866–3873. https://doi.org/10.1021/es204471x.
18. Blundell, T.L., and Jenkins, J.A. (1977). The Binding of Heavy Metal. Chem. Soc. Rev. *6*, 139–171. https://doi.org/10.1039/CS9770600139.
19. Ju, W., Bagger, A., Hao, G.P., Varela, A.S., Sinev, I., Bon, V., Roldan Cuenya, B., Kaskel, S., Rossmeisl, J., and Strasser, P. (2017). Understanding activity and selectivity of metal-nitrogen-doped carbon catalysts for electrochemical reduction of CO_2. Nat. Commun. *8*, 944–949. https://doi.org/10.1038/s41467-017-01035-z.
20. Li, Z., He, D., Yan, X., Dai, S., Younan, S., Ke, Z., Pan, X., Xiao, X., Wu, H., and Gu, J. (2020). Size-Dependent Nickel-Based Electrocatalysts for Selective CO_2 Reduction. Angew. Chem. Int. Ed. Engl. *59*, 18572–18577. https://doi.org/10.1002/anie.202000318.
21. Lees, E.W., Mowbray, B.A.W., Parlane, F.G.L., and Berlinguette, C.P. (2021). Gas diffusion electrodes and membranes for CO_2 reduction electrolysers. Nat. Rev. Mater. *7*, 55–64. https://doi.org/10.1038/s41578-021-00356-2.
22. Weekes, D.M., Salvatore, D.A., Reyes, A., Huang, A., and Berlinguette, C.P. (2018). Electrolytic CO_2 Reduction in a Flow Cell. Acc. Chem. Res. *51*, 910–918. https://doi.org/10.1021/acs.accounts.8b00010.
23. Liu, H., and Fang, H.H.P. (2002). Extraction of extracellular polymeric substances (EPS) of sludges. J. Biotechnol. *95*, 249–256. https://doi.org/10.1016/S0168-1656(02)00025-1.
24. Shi, R., Guo, J., Zhang, X., Waterhouse, G.I.N., Han, Z., Zhao, Y., Shang, L., Zhou, C., Jiang, L., and Zhang, T. (2020). Efficient wettability-controlled electroreduction of CO_2 to CO at Au/C interfaces. Nat. Commun. *11*, 3028. https://doi.org/10.1038/s41467-020-16847-9.
25. Liang, S., Jiang, Q., Wang, Q., and Liu, Y. (2021). Revealing the Real Role of Nickel Decorated Nitrogen-Doped Carbon Catalysts for Electrochemical Reduction of CO_2 to CO. Adv. Energy Mater. *11*, 1–14. https://doi.org/10.1002/aenm.202101477.
26. Zhecheva, E., Stoyanova, R., and Shinova, E. (2007). EPR analysis of the local structure of Ni^{3+} ions in Ni-based electrode materials obtained under high-pressure. J. Mater. Sci. *42*, 3343–3348. https://doi.org/10.1007/s10853-006-0744-x.
27. Vuong, T.H., Rockstroh, N., Bentrup, U., Rabeah, J., Knossalla, J., Peitz, S., Franke, R., and Brückner, A. (2021). Role of Surface Acidity in Formation and Performance of Active Ni Single Sites in Supported Catalysts for Butene Dimerization: A View inside by Operando EPR and In Situ FTIR Spectroscopy. ACS Catal. *11*, 3541–3552. https://doi.org/10.1021/acscatal.0c04894.
28. Li, J., Jiang, Y.F., Wang, Q., Xu, C.Q., Wu, D., Banis, M.N., Adair, K.R., Doyle-Davis, K., Meira, D.M., Finfrock, Y.Z., et al. (2021). A general strategy for preparing pyrrolic-N_4 type single-atom catalysts via pre-located isolated atoms. Nat. Commun. *12*, 6806. https://doi.org/10.1038/s41467-021-27143-5.
29. UN-Habitat (2008). Global Atlas of excreta, wastewater sludge and biosolids management: moving forward the sustainable and welcome uses of a global. http://esa.un.org/iys/docs/san_lib_docs/habitat2008.
30. Report on the Elemental Analyses of Samples from the Targeted National Sewage Sludge Survey (2021 (United States Environmental Protection Agency). https://www.epa.gov/sites/default/files/2021-04/documents/tnsss-appendix-elemental-analyses-report.pdf.
31. US Environmental Protection Agency (2017). Inventory of U.S. Greenhous Gas Emissions and Sinks (1990–2015). https://www.epa.gov/ghgemissions/inventory-us-greenhouse-gas-emissions-and-sinks.
32. Chen, J., Li, C., and Shi, G. (2013). Graphene materials for electrochemical capacitors. J. Phys. Chem. Lett. *4*, 1244–1253. https://doi.org/10.1021/jz400160k.
33. Capodaglio, A., and Olsson, G. (2019). Energy Issues in Sustainable Urban Wastewater Management: Use, Demand Reduction and Recovery in the Urban Water Cycle. Sustainability *12*, 266. https://doi.org/10.3390/su12010266.
34. TRADING ECONOMICS data. https://tradingeconomics.com/commodity/nickel.
35. ChemAnalysts data. https://www.chemanalyst.com/Pricing-data/hydrogen-1165.

STAR★METHODS

KEY RESOURCES TABLE

REAGENT or RESOURCE	SOURCE	IDENTIFIER
Chemicals, peptides, and recombinant proteins		
Wastewater sludge	Luofang wastewater treatment plant of Shenzhen, China	N/A
$H_2IrCl_6 \cdot xH_2O$	Sigma-Aladdin	N/A
BCA kit	Thermo Scientific	N/A
Ni electroplating wastewater	Zhongchuang electroplating Co. Ltd. of Huizhou, China	N/A
GDE_{EPS}	This paper	GDE_{EPS}

RESOURCE AVAILABILITY

Lead contact

Further information and requests can be directed to the lead contact, Lu Lu (lulu@hit.edu.cn).

Materials availability

There are restrictions to the availability of the prepared GDE_{EPS} used in this study due to the claimed filed China patent ZL202210841460.1.

Data and code availability

- Collected data on the figure and table, and detailed data of the prepared GDEs reported in this paper will be shared by the lead contact upon request.
- The article does not report any new code.
- Any additional information required to reanalyze the data reported in this paper is available from the lead contact upon request.

EXPERIMENTAL MODEL AND STUDY PARTICIPANT DETAILS

This study does not use any experimental model.

METHOD DETAILS

EPS extraction from sludge

WAS with ~98% moisture content was obtained from a wastewater treatment plant in Shenzhen. EPS was extracted using modified alkali-aldehyde extraction method.[20] Briefly, 6 mL acetaldehyde (35 wt%) were added into 300 mL sludge under icy bath and stir for 1 h, followed by adding 120 mL NaOH solution (1 M) for another 12 h reaction, finally, the dialysis of supernatant for 100 h to obtain solution containing EPS (~3 $g \cdot L^{-1}$) with molecular weight more than l000 Dalton. The frozen-dried EPS was in faint-yellow (Figure S2).

Treatment of the Ni-contained electroplating wastewater

Ni-contained electroplating wastewater was a combined wastewater obtained from a factory in Meizhou, Guangdong Province. Content and concentration of the main heavy metals in the electroplating wastewater were presented in Table S1. The raw 1 L wastewater was added with concentrated HNO_3 to adjust solution pH below 1. The acidified wastewater was followed by heated at 85°C for 1 h and then added with 50 mL 30% H_2O_2. This process was used to dissolve metal particles in the flocs in the wastewater. Then the wastewater filtered by a qualitative filter paper to exclude other particles or flocs. And the solution pH was then adjusted to 6-8 by 3 M NaOH addition.

GDE fabrication based on electrospinning

One electrospinning solution containing EPS-Ni ligands was prepared by mixing Ni-contained electroplating wastewater (Table S1) with EPS solution, followed by ultrasonication (details in Supporting Information, SI). The mass ratio of EPS : Ni is around 50 : 1. Another electrospinning solution is 12 wt% polyacrylonitrile (PAN) served as a supporting material of membrane in N'N-Dimethylformamide (DMF). Two spinning solutions were separately injected into an electrospinning machine (TL-Pro-BM2020, Tongli Tech, China) with a roller collector of 10 cm in diameter and 15 cm in length by using a voltage of 16~22 kV at the two syringes and ~ -4 kV at the roller collector. The mass ratio of EPS to PAN is 1:1. The pristine GDE (Figure S3) was fabricated by 40~50 h electrospinning, which was then pre-oxidized at 260°C in a muffle furnace, followed by carbonization at 1000°C in a tube furnace under argon atmosphere protection. Finally, carbonized GDE_{EPS} was coated by a layer of

polytetrafluoroethylene (PTFE) as the hydrophobic layer. Since protein is the dominant content of EPS (Table S2), pure protein of bovine serum albumin (BSA) was employed as a control of matrix to combine Ni for manufacturing GDE named GDE_{PR}.

EPS as a very complex organic mainly consists of protein, polysaccharide and humic acid (Table S2). In order to investigate their roles on the coordination of SACs and the corresponding ECO_2RR performance, we individually employed EPS, protein, polysaccharide and humic acid as matrixes to anchor Ni to produce the ECO_2RR catalysts by using the similar process as manufacture of carbonized GDE without PTFE layer, but the GDEs were milled to powdery catalysts that are convenient for electrochemical tests. A blank of catalyst containing supporting material of PAN only (without any matrix) was prepared. To exclude the impact of N-doping, we also prepared another control of catalyst without N element by using N-free polyvinyl alcohol (PVA), another supporting material as PAN, to mix with N-free polysaccharide for production of Polysaccharide+PVA catalyst.

PTFE layer preparation

60% polytetrafluoroethylene concentrated dispersions were brushed onto one surface of the GDE_{EPS} and dried out naturally. The GDE_{EPS} was heated in a furnace at 320°C for 10 minutes to allow the formation of PTFE layer.

ECO_2RR experiment

The ECO_2RR performance of GDE_{EPS} and GDE_{PR} served as cathodes was tested in a customized membrane electrode assembly (MEA) with an IrO_2-coated titanium mesh anode and a Fumasep-FAA-30 anion exchange membrane separator (Figure 3). The CO_2 gas was injected into the cathode with a flow of 20~50 standard cubic centimeter per minute (sccm). The anolyte is the 0.5 M $KHCO_3$ solution that was circulated by a peristaltic pump. The performance of catalysts derived from different composition of EPS was tested in a traditional single-chamber three-electrode electrochemical cell with a platinum counter electrode, an Ag/AgCl reference electrode and a carbon paper (Tory TGP-H-060) working electrode with normalized 2 $mg \cdot cm^{-2}$ catalyst powder loading. All electrochemical experiments were carried out using a potentiostat (1010E, Gamry, USA).

GDE characterizations

Scanning electron microscopy (SEM) (TESCAN MIRA4), transmission electron microscopy (TEM) (FEI Talos F200X), and X-ray diffraction (XRD) (RIGAKU Ultima IV) were used to characterize the morphology and structure of GDE. Aberration-corrected scanning transmission electron microscopy (AC-STEM) (Titan Cubed Themis G2300) was used to identify Ni SAs. Porous structure was analyzed by a BET analyzer (Micrometrics ASAP 2460) using N_2, and CO_2 gas was also applied to examine material's CO_2 storage ability. The hydrophilic or hydrophobic nature of GDE's surface was characterized by contact angle (KRUSS DSA25; Dingsheng JY-82) and the aqueous penetration that was probed by a confocal laser scanning microscope (Nikon AX-SHR). Heavy metals species and content were identified by an inductively coupled plasma mass spectrometry (NexION 1000, PerkinElmer). Chemical bonds and compositions were analyzed by an X-ray photoelectron spectroscopy (XPS) (Scientific K-Alpha). Gas products were identified and quantified by a gas chromatography equipped with a thermal conductivity detector (TRACE 1310, Thermo, USA). The liquid products were identified by a proton nuclear magnetic resonance (NMR) at 400 MHz (Bruker Avance NEO). The X-ray absorption near-edge spectroscopy (XANES) and extended x-ray absorption fine structure spectroscopy (EXAFS) were collected at a beamline BL44B2 by the SPring-8 synchrotron in Japan. The storage rings of SPring-8 were operated at 8.0 GeV with a maximum current of 250 mA. Using Si (111) double-crystal monochromator, the data collection was carried out in transmission mode using ionization chamber. The k^3-weighted EXAFS spectra were obtained by subtracting the post-edge background from the overall absorption and then normalizing with respect to the edge-jump step. Subsequently, k^3-weighted $\chi(k)$ data of Ni K-edge were Fourier transformed to real (R) space using a Hanning window (dk=1.0 $Å^{-1}$) to separate the EXAFS contributions from different coordination shells. All spectra were collected in ambient conditions. The chemical valent of Ni SAs was detected by electron paramagnetic resonance (EPR) (EMXnano, Bruker, Germany) with magnetic field between 100-600 mT. The surface electro-activity of GDE_{EPS} was characterized by a scanning electrochemical microscopy (SCEM) (Versascan, Ametek) equipped with a position system, two potentiostats (VersaSTAT 3/3F) and a microprobe (ϕ 25 μm Pt microprobe) using substrate generation/tip collection (SG/TC) model. All details in material characterization were provided in SI.

Measurement of protein, polysaccharide and humic acid content in EPS

Protein was colored by standard BCA kit (Pierce™ BCA Protein Assay Kit, Thermo Scientific, USA), and an enzyme-labeled instrument (Synergy H1, Biotek, USA) was employed to detect protein content at 562 nm. Phenol-sulfuric acid method was applied to detect the content of polysaccharide by an UV-Vis spectrophotometer (GENESYS 150, Thermo Scientific, USA) at 485 nm. Folin-Lowry method detected humic acid content by an UV-Vis spectrophotometer at 735 nm.

Calculations

Potentials reported in this study versus reversible hydrogen electrode (RHE) were derived from converting detected values according to Nernst equation:

$$E\ vs\ RHE = E\ vs\ Ag/AgCl + 0.197 + 0.059 \times pH$$

Partial current density for given gas products was calculated by the following formula:

$$j_i = x_i \times v \times z_i \times F \times P_0 \times electrode\ area\ /\ (RT)$$

Where, j_i (mA·cm^{-2}) is the partial current density; x_i (ppm) is the volume fraction of given gas product i; v (sccm) is the flow rate; z_i is the number of transferred electrons; F (C·mol^{-1}) is the Faraday constant; P_0 equals to 101.325 kPa; R (J·mol^{-1}·K^{-1}) is the gas constant; and T (K) is the temperature. The corresponding Faradic Efficiency (FE, %) was deduced as the follow:

$$FE = j_i\ /\ j_{total} \times 100\%$$

Where, j_{total} (mA·cm^{-2}) is the total current density. Energy efficiency (%) can be calculated as the follows:

$$Energy\ efficiency = (E^0 \times FE_{CO})/E_{cell} \times 100\%$$

$$E^0 = E_{O2} - E_{CO} = 1.23\ V - (-0.11\ V) = 1.34\ V$$

Where, E_{O2} (V) and E_{CO} (V) are O_2/H_2O and CO_2/CO equilibrium potential, respectively; E_{cell} is a voltage applied to the MEA.

Evaluation of turnover frequency (TOF)

TOFs(h^{-1}) for ECO_2RR products were evaluated based on the electrochemical active surface area (ECSA) normalization proposed by Jiang et al.[5] and Chen et al.[32] The ECSA results were presented in Table S3, which were calculated according to 21 μF·cm^{-2} of reported electrochemical double layer capacity (EDLC) of graphene. Then the moles of C atoms were estimated by the formula: ESCA/(specific surface area)×12 (Table S3). And considering the Ni atomic content in the membrane electrode (XPS result, Table S3). Then TOFs based on ESCA normalization was calculated by (j_{total}×t×FE_{CO})/(2F×the number of Ni sites).

Calculation of potential carbon-foot and economic benefits in practice

The calculations of potential carbon-foot and economic benefits are based on following 4 steps (Figure S23) including the CO_2 feed (Step 1), the preparation of GDE_{EPS} and the conversion of CO_2 (Step 2), electricity input (Step 3) and product separation (Step 4). We consider the emission and fixation of CO_2 during GDE manufacture and electrocatalysis, CO_2 emission associated with electrical energy consumption, the cost of GDE manufacture, and the economic benefits derived from sludge treatment, heavy metal recovery and H_2 production. The energy consumption and cost for the CO_2 capture and CO separation as well as transportation of the raw materials and products were not considered. The detailed calculations were provided as follows:

Carbon footprint

Step 1: In this study, we assumed that a direct feed of anaerobic digestion biogas (30-40% CO_2) to the electrocatalytic process. We did not consider the cost of the purification of CO_2, and thus no emission or conversion or fixation of CO_2 occurred in the Step 1. The CO_2 emission was 0 ton-CO_2-eq/ton-CO-produced.

Step 2: This step calculated the fixed CO_2 in GDE_{EPS} and converted CO_2. Globally, annual ~30.79 million tons sludge (dry weight) were produced in major economies, meaning that ~15.4 million tons EPS could be reclaimed given ~50 wt% biomass ratio in the sludge.[29,30] The medium C and N content in dry biomass are estimated to 31.39 wt% and 3.97 wt%,[30] equaling to 4.83 million tons C-eq/year or 17.72 million tons CO_2-eq/year 0.61 million tons N-eq/year. The CO_2 fixed amount is 0.70 ton-CO_2-eq/ton-CO-produced.

For the converted CO_2, the durability of each GDE_{EPS} is set at 4 h and 70% FE_{CO} and 30% FE_{H2} are considered as the average value when current operation is under 40 mA/cm^2. Therefore, one ton EPS annually capturing CO_2 amount can be calculated as the following equation:

$$CO_2\ capture\ amount = x_{CO} \times v \times 60 \times 24 \times 365\ /\ [EPS\ amounts\ in\ per\ cm^2 \times (365 \times 24\ /\ 4)]$$

Where, x_{CO} is the volume fraction of CO; v (sccm) is the CO_2 flow rate; EPS amount in one cm^2 is as follows:

$$EPS\ amount\ in\ per\ cm^2 = EPS\ addition\ during\ electrospinning\ /\ (pristine\ GDE_{EPS}\ area \times contraction\ factor)$$

Where, the pristine GDE_{EPS} is ~450 cm^2 (the GDE collector was a roller in diameter of 10 cm and in width of 15 cm) with 10 g EPS as the matrix. After preoxidation and carbonization, the final GDE_{EPS} shrinks to around 30% in size of the pristine one, thus the contraction factor is 0.7.

The optimal C capture can come to 40.02 million tons CO_2-eq/year or 1.57 ton-CO_2-eq/ton-CO-produced. 0.03 ton-H_2-eq/ton-CO-produced can be harvested at the same time.

Step 3: This step calculated the energy-related CO_2 emission which was used for the manufacture of GDE_{EPS} and CO_2-CO conversion. And the energy was derived from the combustion of fossil fuels. According to the energy limitation to produce common graphene (6440 kW·h/ton), carbonizing annual EPS yield into GDE_{EPS} (mass ratio of EPS : PAN is 1:1) consumed 15.4 million tons × 2 × 6440 kW·h/t = 198.36 billion kW·h, relative to 24.38 million tons standard coal combustion and 65.58 million tons CO_2 emission or 2.58 ton-CO_2-eq/ton-CO-produced (1 kW·h electricity generation needs 0.1229 kg standard coal combustion, and the combustion of 1-ton standard coal equaled 2.69 tons CO_2 emission based on the proposed value of 2.66-2.72 tons CO_2 emission from the combustion of 1-ton standard coal, this data was suggested by Nation Development and Reform Commission of China and National Bureau of Statistics). However, this

data can be further decreased to 1.52 ton-CO_2-eq/ton-CO-produced considering that only 58.9% energy was from the combustion of fossil fuels in the electricity grid.

The energy input for converting CO_2 to CO was based on the energy efficiency (EF, 52.34%) and the relationship between the change of Gibbs free energy and electromotive force:

$$\Delta G = -n \cdot F \cdot E$$

$$W = \Delta G / EF \times converted\ CO_2$$

Where, ΔG (J) is the change of Gibbs free energy; n is the number of transferred electrons (2); F is Faradic constant (96485 C/mol) E is the electromotive force between CO and CO_2 (-0.11 V); W is the real energy for CO_2 to CO (10.25 billion kW·h). The corresponding CO_2 emission was 3.39 million tons CO_2-eq/year or 0.13 ton-CO_2-eq/ton-CO-produced. And it can be decreased to 0.08 ton-CO_2-eq/ton-CO-produced given the current electricity mix.

Step 4: This study did not consider the cost and energy for the separation/purification of the produced CO and H_2, and thus the emission or fixation/conversion of CO_2 was 0 ton-CO_2-eq/ton-CO-produced in the Step 4.

Total CO_2 fixation or conversion: Step 1 + Step 2 – Step 3 + Step 4 = 0 + 0.7 + 1.57 – 1.52 – 0.08 + 0 = 0.67 ton-CO_2-eq/ton-CO-produced.

Economic benefits

Step 1: In this study, CO_2 was from the fermenters of sludge or wastewater. We did not consider the cost of the purification of CO_2, no cost or economic yield was generated.

Step 2: The cost of manufacture of GDE_{EPS} and electrolysis includes the expenditure for PAN and the energy. The cost of PAN is 1234 US$/ton, equaling to ~752 US$/ton-CO-produced (mass ratio of PAN : EPS is 1 : 1). Total energy input is 208.61 billion kW·h (198.36 billion kW·h for GDE_{EPS} manufacture and 10.25 billion kW·h for CO_2-CO conversion) means 37.34 billion US$ for electricity considering the average price of electricity of 0.179 US$/kW·h globally. The corresponding energy cost of one ton produced CO is ~1466 US$/ton-CO-produced.

Step 3: Some revenues can also be generated from the alternatives from sludge treatment, Ni recovery and byproducts H_2. The average cost of sludge treatment is ~205 US$/ton,[33] which equals to ~248 US$/ton-CO-produced. Based on the mass ratio of 1 : 1of EPS : Ni, around 0.31 million tons Ni can be recovered annually, which equals ~243 US$/ton-CO-produced considering the cost of Ni is 20000 US$/ton-Ni.[34] The average price of H_2 is 6500 US$/ton-$H_2$.[35] which equals to revenue of ~199 US$/ton-CO-produced.

Step 4: This study did not consider the cost and energy for the separation/purification of the produced CO and H_2, and thus no cost or economic yield was generated in the Step 4.

The cost for producing one ton CO in this study was estimated to be: 752 + 1466 = 2218 US$/ton-CO-produced. The potential economic from the waste recovery (sludge and heavy metals) and H_2 generation was estimated to be: 248 + 243 + 199 = 690 US$/ton-CO-produced. The global price of CO is 3337 US$/ton-CO. Thus, the total economic benefits for producing ton CO were to be estimated: 3337 + 690 – 2218 = 1809 US$/ton-CO-produced.

QUANTIFICATION AND STATISTICAL ANALYSIS

The presented data in this paper are in average value ± SD with triplication.